JOURNAL OF GEOPHYSICAL RESEARCH, VOL. 115, A07102, doi:10.1029/2009JA014854, 2010

Comparative analysis and variability of the Jovian X-ray spectra detected by the Chandra and XMM-Newton observatories

Yawei Hui,[1] David R. Schultz,[1] Vasili A. Kharchenko,[2] Anil Bhardwaj,[3] Graziella Branduardi-Raymont,[4] Phillip C. Stancil,[5] Thomas E. Cravens,[6] Carey M. Lisse,[7] and Alexander Dalgarno[8]

Received 31 August 2009; revised 12 January 2010; accepted 19 February 2010; published 8 July 2010.

[1] Expanding upon recent work, a more comprehensive spectral model based on charge exchange induced X-ray emission by ions precipitating into the Jovian atmosphere is used to provide new understanding of the polar auroras. In conjunction with the Xspec spectral fitting software, the model is applied to analyze observations from both Chandra and XMM-Newton by systematically varying the initial precipitating ion parameters to obtain the best fit model for the observed spectra. In addition to the oxygen and sulfur ions considered previously, carbon is included to discriminate between solar wind and Jovian magnetospheric ion origins, enabled by the use of extensive databases of both atomic collision cross sections and radiative transitions. On the basis of fits to all the Chandra observations, we find that carbon contributes negligibly to the observed polar X-ray emission suggesting that the highly accelerated precipitating ions are of magnetospheric origin. Most of the XMM-Newton fits also favor this conclusion with one exception that implies a possible carbon contribution. Comparison among all the spectra from these two observatories in light of the inferred initial energies and relative abundances of precipitating ions from the modeling show that they are significantly variable in time (observation date) and space (north and south polar X-ray auroras).

Citation: Hui, Y., D. R. Schultz, V. A. Kharchenko, A. Bhardwaj, G. Branduardi-Raymont, P. C. Stancil, T. E. Cravens, C. M. Lisse, and A. Dalgarno (2010), Comparative analysis and variability of the Jovian X-ray spectra detected by the Chandra and XMM-Newton observatories, *J. Geophys. Res.*, *115*, A07102, doi:10.1029/2009JA014854.

1. Introduction

[2] Since the first detection of X rays from Jupiter by the Einstein observatory in the 1980s [*Metzger et al.*, 1983], debate has persisted regarding the mechanism by which this emission arises. Owing to the limited spatial and spectral resolution of the first generation of X-ray satellites, observations in the X-ray band of 0.1–1 keV [*Waite et al.*, 1994; *Gladstone et al.*, 1998] were insufficient to distinguish between the models seeking to explain them (cf. *Bhardwaj and Gladstone* [2000] for discussion). With the tremendous improvement in both spatial and spectral resolution in the past decade owing to the latest generation of observatories (i.e., Chandra and XMM-Newton) several, much more precise, measurements of the Jovian X-ray emission have been made [*Gladstone et al.*, 2002; *Elsner et al.*, 2005; *Branduardi-Raymont et al.*, 2004, 2007a, 2007b, 2008; *Bhardwaj et al.*, 2005, 2006]. There is now strong evidence that there are two distinct components of the Jovian soft X-ray emission, one from the high latitudes (north and south polar X-ray auroras) and the other from lower latitudes and the equatorial regions (the so-called disk component). The major source of the disk component is the scattering and fluorescence of solar X rays in the atmosphere [*Maurellis et al.*, 2000; *Branduardi-Raymont et al.*, 2007b; *Bhardwaj et al.*, 2005, 2006; *Cravens et al.*, 2006]. In contrast, the main auroral soft X-ray (<2 keV) component is thought to be charge exchange induced X rays that arise from energetic heavy ions which precipitate into the Jovian upper atmosphere [*Metzger et al.*, 1983; *Horanyi et al.*, 1988; *Waite et al.*, 1994; *Cravens et al.*, 1995, 2003], while at higher energies (>2 keV) bremsstrahlung by electron precipitation dominates [*Branduardi-Raymont et al.*, 2007a].

[1]Physics Division, Oak Ridge National Laboratory, Oak Ridge, Tennessee, USA.
[2]Physics Department, University of Connecticut, Storrs, Connecticut, USA.
[3]Space Physics Laboratory, Vikram Sarabhai Space Center, Trivandrum, India.
[4]Mullard Space Science Laboratory, University College London, Surrey, UK.
[5]Department of Physics and Astronomy and the Center for Simulational Physics, University of Georgia, Athens, Georgia, USA.
[6]Department of Physics and Astronomy, University of Kansas, Lawrence, Kansas, USA.
[7]Johns Hopkins University Applied Physics Laboratory, Laurel, Maryland, USA.
[8]Harvard-Smithsonian Center for Astrophysics, Cambridge, Massachusetts, USA.

0148-0227/10/2009JA014854

[3] Regarding the auroral soft X-ray spectra, a series of observations and analyses have been carried out to infer the compositions of the precipitating ion fluxes [e.g., *Elsner et al.*, 2005; *Branduardi-Raymont et al.*, 2004, 2007a, 2007b], while theoretical modeling based on simulations of the emission following charge exchange between heavy ions and molecular hydrogen has been developed to constrain the ion energies and abundances at the top of the Jovian atmosphere [*Metzger et al.*, 1983; *Horanyi et al.*, 1988; *Waite et al.*, 1994; *Cravens et al.*, 1995; *Kharchenko et al.*, 1998; *Liu and Schultz*, 1999; *Kharchenko et al.*, 2006, 2008]. It has been established that highly charged oxygen and sulfur ions with MeV/u initial energies can account for the observed line emissions in the Chandra and XMM-Newton spectra. However, the origin of these ions is still unclear. *Cravens et al.* [2003] proposed two possible sources for the heavy ions that lead to the Jovian X-ray auroras: (1) solar wind ions entering into the magnetospheric polar cusps and (2) ambient sulfur and oxygen ions accelerated in the outer magnetosphere by large field-aligned potentials. In addition, *Bunce et al.* [2004] suggested that pulsed magnetic reconnection on the dayside Jovian magnetopause produces bipolar field-aligned currents that would, for certain solar wind conditions, accelerate magnetospheric ions. To distinguish between these two ion sources and to seek better constraints on other characteristics such as the ion acceleration mechanism, we have improved and extended our recent spectral model [*Kharchenko et al.*, 2008] and added the contribution of carbon ions, the most abundant heavy element in the solar wind after oxygen.

[4] Here, we describe in detail the new precipitation model (section 2), synthetic spectra (sections 3 and 4), and fits to the XMM-Newton observations made by *Branduardi-Raymont et al.* [2004, 2007a] (section 5). We also present an expanded analysis of the Chandra observations [*Elsner et al.*, 2005] that we recently reported [*Hui et al.*, 2009] and compare and discuss the results from both sets of observations (section 6).

2. Charge Exchange Induced X-Ray Emission Model

[5] The collisions of precipitating ions with neutral gas molecules (principally molecular hydrogen) and the consequent X-ray emission take place in the Jovian upper atmosphere. Early charge exchange (CX) models only accounted for oxygen ion precipitation [*Cravens et al.*, 1995; *Kharchenko et al.*, 1998; *Liu and Schultz*, 1999] because of the lack of the extensive atomic data required (e.g., energy-dependent, state-selective CX cross sections for all ionization stages of the ions). Large-scale atomic collision [*Schultz et al.*, 2009] and structure calculations enabled the recent addition of sulfur [*Kharchenko et al.*, 2006, 2008] and now carbon [*Hui et al.*, 2009]. Inclusion of these three ion species allows the first level of discrimination between Jovian magnetospheric (S and O) and solar wind (O and C) origin of the ions. The soft X-ray photons emitted after CX are assumed to escape freely from the atmosphere (i.e., the optical depth is much less than unity) (N. Ozak et al., Auroral X-ray emission at Jupiter: Depth effects, submitted to *Journal of Geophysical Research*, 2010).

[6] In our model, an ion precipitates into the Jovian atmosphere losing energy in collisions with neutral gas and capturing electrons into excited states that subsequently decay. The model includes the dominant reaction channels that lead to deexcitation of ion electronic levels via photon emissions and to changes in ion kinetic energy. These include CX, electron stripping of the precipitating ions (STRP), and ionization (ION) of the neutral gas. CX changes the ion charge, q, through capture of a single electron, capture of an electron with simultaneous ionization of the other electron in H_2, or capture of two electrons with subsequent autoionization of one of the electrons. Each of these CX processes leads to the charge changing by one, $q \rightarrow q - 1$ and, for simplicity, their sum is referred to as CX here. Rarely, two electrons can be captured into a state that does not autoionize and these events are neglected in the present model. Stripping increases the ion charge ($q \rightarrow q + 1$) and only removal of a single electron is considered. Ionization without CX does not change the ion charge ($q \rightarrow q$) and so does not lead to X-ray emission but is the principal kinetic energy loss process for the precipitating ions. We show in Figure 1a the channel probabilities (CX, STRP, ION) for $C^{5+} + H_2$ as an example and note that CX dominates at low collision energies and ION at high collision energies. Also for illustration, Figure 1b shows the collision energy dependence of the CX cross sections for capture to the most frequently populated levels of C^{4+} in the collision $C^{5+} + H_2$.

[7] The model is divided into two independent modules, one to track the result of the collisions suffered during the precipitation and the other to track the deexcitation cascade from the CX-generated ion level populations and the resulting photon spectrum.

2.1. Monte Carlo Collision Module

[8] To begin with, the precipitation and deceleration of ions for each elemental species considered (C, O, and S) are simulated in a Monte Carlo (MC) approach keeping track of the ion charge state and energy at each collision event until an ion has slowed sufficiently that further collisions have a negligible likelihood of producing a state that can lead to X-ray emission. At the conclusion of the simulation the number of events for each charge state (q) are binned according to the ion energy (E) with a bin size of ΔE = 20 keV/u yielding the CX collision number distribution, $N^{CX}(q, E)$. In Figure 2, we show an example of this distribution for each elemental species. Using $N^{CX}(q, E)$, instead of the energy and charge distributions approach adopted in previous modeling [*Cravens et al.*, 1995; *Liu and Schultz*, 1999], allows a fully collision energy-dependent photon yield to be computed.

[9] We consider a series of initial ion energies in the range of 0.02–2 MeV/u and for each energy we run a MC simulation to determine the CX collision number distribution. Figure 3 shows a comparison of $N^{CX}(q, E)$ for three charge states of oxygen (q = 6, 7, 8) with different initial ion energies (E_{init} = 1 and 2 MeV/u). We find that varying the initial ion energy does not change the overall shape of $N^{CX}(q, E)$, but it has a significant effect on the ion distribution by cutting off the distribution beyond the initial ion energy (see, for example, the missing tail of $N^{CX}(q, E)$ for O^{6+} at 1 MeV/u compared to that for 2 MeV/u in Figure 3).

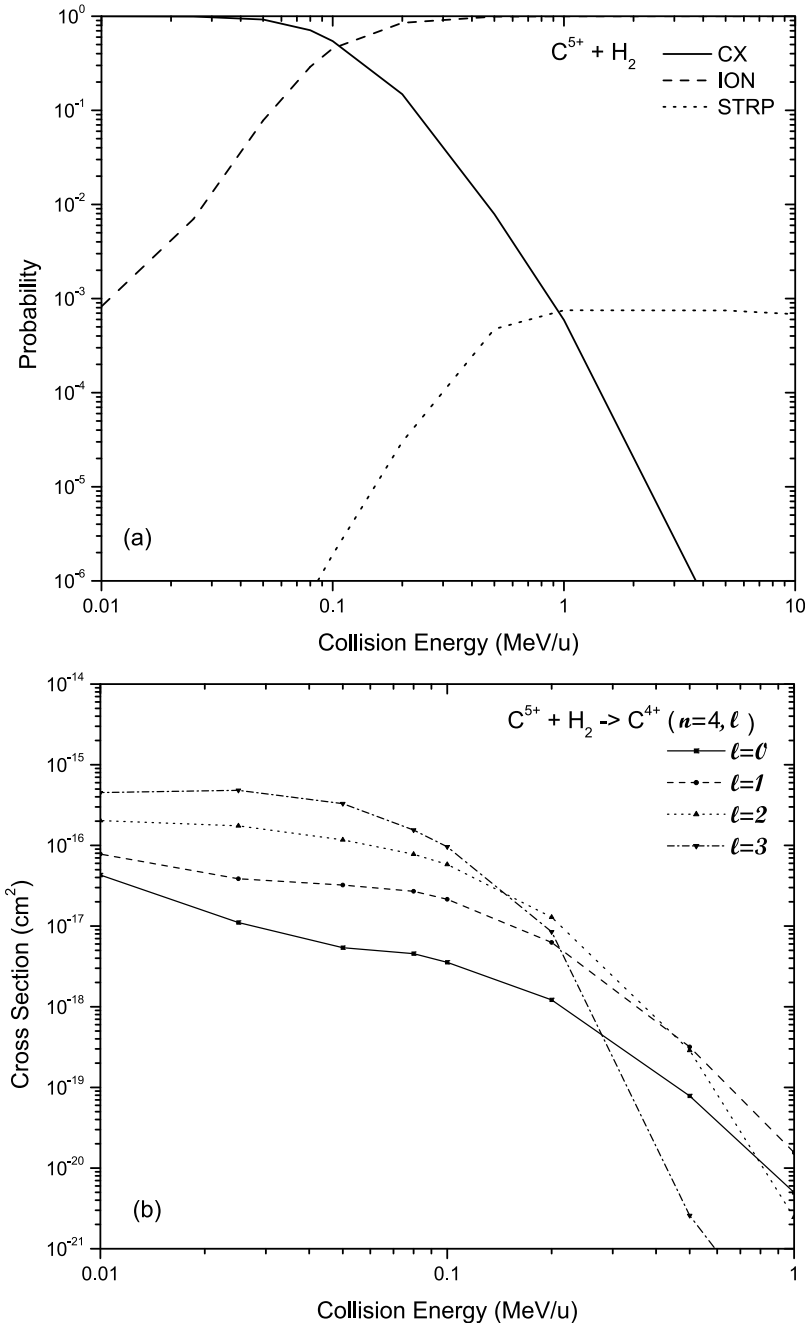

Figure 1. Example of the atomic collision data [*Schultz et al.*, 2009] used in the present charge exchange induced X-ray emission modeling. (a) The probability as a function of collision energy for C^{5+} impact of H_2 for charge exchange (CX, the sum of single electron capture, transfer ionization, and double electron capture with autoionization), ionization of the molecular hydrogen target (ION), and stripping of the carbon ion (STRP, $C^{5+} \rightarrow C^{6+}$). (b) A portion of the state-selective CX cross sections (n = 4, ℓ = 0,1,2, and 3) for $C^{5+} + H_2$.

Unlike the changes resulting from using different initial ion energies, we find that varying the initial ion charge (q_{init}) or varying the total number (N_{tot}) of ions in the simulation has a minimal effect on the distribution function. We therefore adopt $q_{\mathrm{init}} = 1$ and $N_{\mathrm{tot}} = 1000$ for all subsequent calculations.

[10] The tabulated state-selective CX collision cross sections [*Schultz et al.*, 2009] (see Figure 1b, for example) are also needed to obtain the initial population of excited states following charge exchange, where γ labels a particular level with the single-electron quantum numbers n and ℓ. Since the tabulated data only extend in energy up to 1 MeV/u and previous analysis [*Cravens et al.*, 2003; *Kharchenko et al.*, 2006, 2008] has suggested that the initial ion energies could be as high as several MeV/u in order to generate sufficient X-ray power to account for the observed flux, we have (linearly) extrapolated the cross

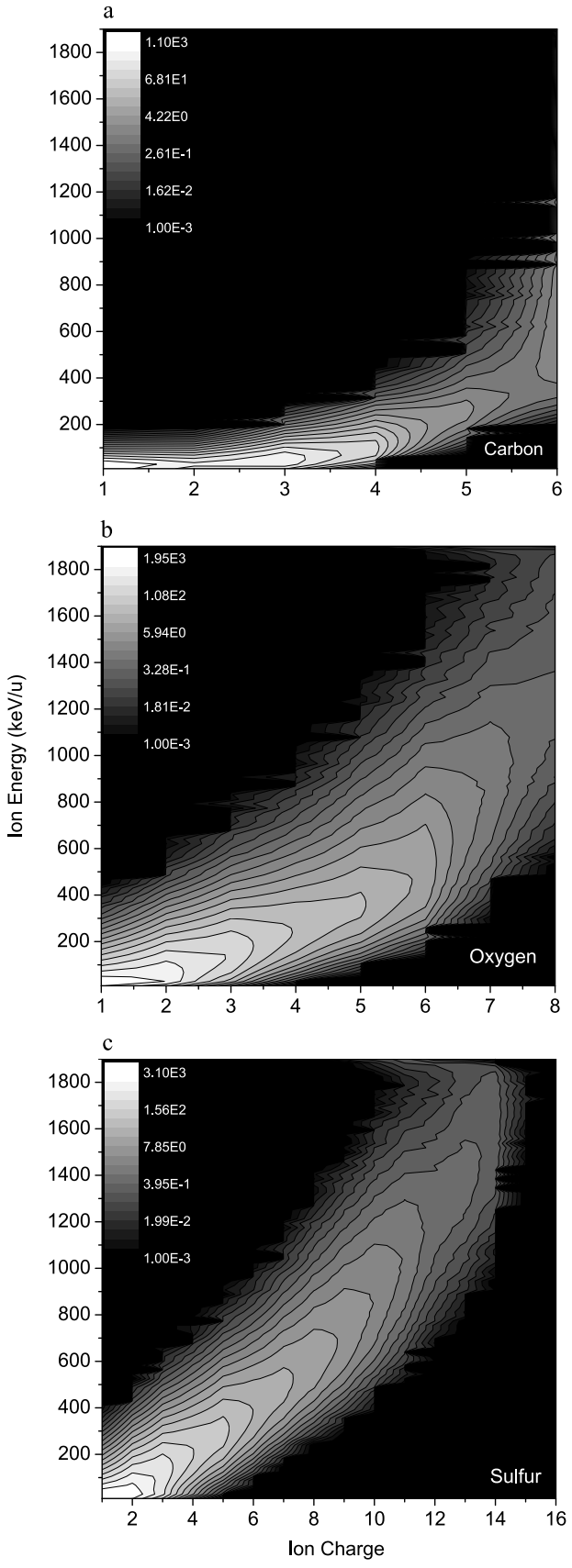

Figure 2. Charge exchange collision number distribution, $N^{CX}(E, q)$ for each element is shown as a contour map. The calculations were carried out with N_{tot} = 1000, q_{init} = 1, and E_{init} = 2 MeV/u. The distribution has been binned with ΔE = 20 keV/u and the collision number at a given ion charge and energy is averaged over the total ion number.

sections to 2 MeV/u using the highest two tabulated energy points and made a test calculation to confirm that it is reasonable. For example, for highly charged ions that emit X rays important collision energy ranges are 0.1–1 MeV/u, 0.5–1.2 MeV/u, and 0.8–1.6 MeV/u for carbon ($C^{4+,5+,6+}$), oxygen ($O^{6+,7+,8+}$), and sulfur (S^{9+}–S^{16+}), respectively.

2.2. Photon Emission Module

[11] Having the state-selective CX collision number distribution the second module required to generate the synthetic spectrum involves determining the deexcitation pathway from any initially populated excited state to any final state, including those that result in X-ray emission. That is, we next compute the transition matrix $T(q;\gamma', \gamma)$ connecting the initial (γ) and final (γ') states [*Kharchenko et al.*, 1998; *Kharchenko and Dalgarno*, 2000]. In addition to the prominent transitions used previously, here we collected a large data set from the NIST Atomic Spectra Database (http://physics.nist.gov/asd3), the Atomic Line List (http://www.pa.uky.edu/~peter/atomic/), and recent results for several ion species [*Johnson et al.*, 2002; *Kingston et al.*, 2002; *Nahar*, 2002]. An illustration of the transitions (Grotrian diagram) for the S XII doublet is shown in Figure 4.

[12] Because the initial populations of excited states of the ions produced in the CX model are only (n, ℓ)-resolved, we made the following simplifying approximations: (1) in calculating the multiplet-averaged transition rates and energies, we adopted the approach used by *Johnson et al.* [2002] to account for the fine structure substates; and (2) in populating the "core-excited" energy levels (e.g., $2s2p(^3P)3d(^2D)$), in contrast to the "shell-excited" levels (e.g., $2s^23d(^2D)$), we assigned splitting factors to the energy levels that distribute the total initial populations among both "shell-excited" and "core-excited" energy levels according to their statistical weights. Our atomic transition data set is almost entirely composed of E1 (electric dipole) transitions with several intercombination and forbidden transitions for helium-like C, O, and S (see *Johnson et al.* [2002], *Kingston et al.* [2002], and *Nahar* [2002] for details). In total, we include 960 carbon, 954 oxygen, and 1512 sulfur emission lines when calculating the transition matrices. For the present soft X-ray spectral synthesis, we consider only transitions with photon energies above 200 eV and this reduces the number of transitions to 23 for carbon, 32 for oxygen, and 384 for sulfur comparing to the 6 for oxygen and 27 for sulfur transitions (with energies above 200 eV) previously included [*Kharchenko et al.*, 2008].

[13] From the excited state populations after CX, $X(q, E; \gamma)$, which are obtained from the state-selective CX collision cross sections, and the transition matrices, we compute the photon yields from the cascade process as $Y(q, E; \gamma', \gamma) = T(q;\gamma', \gamma) \times X(q, E; \gamma)$. The synthetic spectrum, or the total yield of

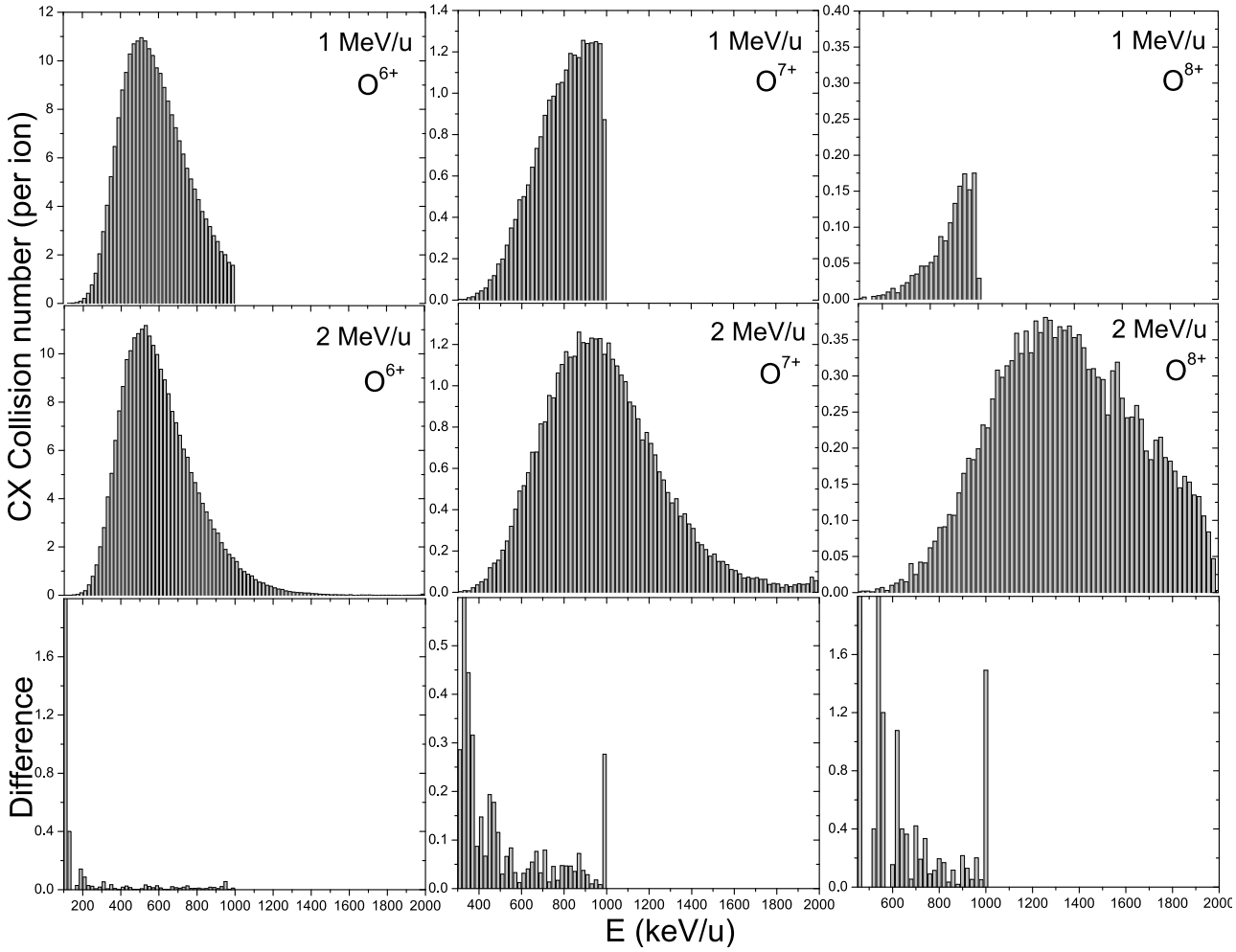

Figure 3. Charge exchange collision number distribution $N^{CX}_{E\text{init}}(q, E)$ for O^{6+}, O^{7+}, and O^{8+} at two different initial energies, 1 and 2 MeV/u, are shown as histograms. They were calculated with N_{tot} = 1000 and q_{init} = 1. The distribution has been binned with ΔE = 20 keV/u and the collision number is averaged by dividing by N_{tot}. The third row shows the difference of the collision number distributions at 1 MeV/u compared to that at 2 MeV/u. This difference is calculated as $Diff = 2 \times abs\ ((N^{CX}_{1\text{MeV/u}} - N^{CX}_{2\text{MeV/u}})/(N^{CX}_{1\text{MeV/u}} + N^{CX}_{2\text{MeV/u}}))$, for $E < 1$ MeV/u.

photons, is calculated as the sum over both charge states and energy bins, that is, $\sum_{q,E} N^{CX}(q, E) \times Y(q, E; \gamma', \gamma)$.

3. Synthetic Spectra Calculations

[14] The output of our model is the relative intensities of X-ray emission lines with zero line widths. To account for the finite instrumental resolution, we assume that the lines possess Gaussian profiles and their width is a free parameter of the fitting to the observed spectra (i.e., the width is set to the same value for all lines included in the model). For illustration, we show in Figure 5 the synthetic spectra with N_{tot} = 1000, q_{init} = 1, and E_{init} = 1.2 MeV/u for equal abundances of precipitating C, O, and S ions. The discrete emission lines are shown as colored points and the solid curves result from the choice of the line width (full width at half maximum, FWHM) of 10 eV. This line width was chosen to be more narrow than that of the observations in order to illustrate clearly the resulting spectral features.

[15] The prominent emission lines include, for example, C VI ($2p \rightarrow 1s$ at 367.1 eV and $3p \rightarrow 1s$ at 435.1 eV); O VIII ($2p \rightarrow 1s$ at 652.7 eV), O VII ($2^1P \rightarrow 1^1S$ at 574 eV and $2^3S \rightarrow 1^1S$ at 561 eV); S IX ($2s^2 2p^3 (^2D) 3s\ ^3D \rightarrow 2s^2 2p^4\ ^3P$ at 223.2 eV, $2s^2 2p^3 (^2D) 3s\ ^1D \rightarrow 2s^2 2p^4\ ^1D$ at 228.2 eV). Because of its large atomic number, even low charge states of the sulfur ions have the potential to contribute to the X-ray emission, whereas only the highest ionization stages of oxygen and carbon ions can yield X-ray photons. We also note that in the soft X-ray band, while the oxygen ions contribute mainly in the range of 550–850 eV, carbon and sulfur have their most prominent emissions between 300–500 eV and 150–400 eV, respectively. For photon energies below 100 eV, carbon ions generate relatively more flux than do oxygen and sulfur ions, which have similar contributions.

[16] We next illustrate the effect on the synthetic spectra resulting from variation of the initial ion energy by displaying, in Figure 6, a series of model spectra again with C, O, and S in equal abundance and with a line width of 10 eV.

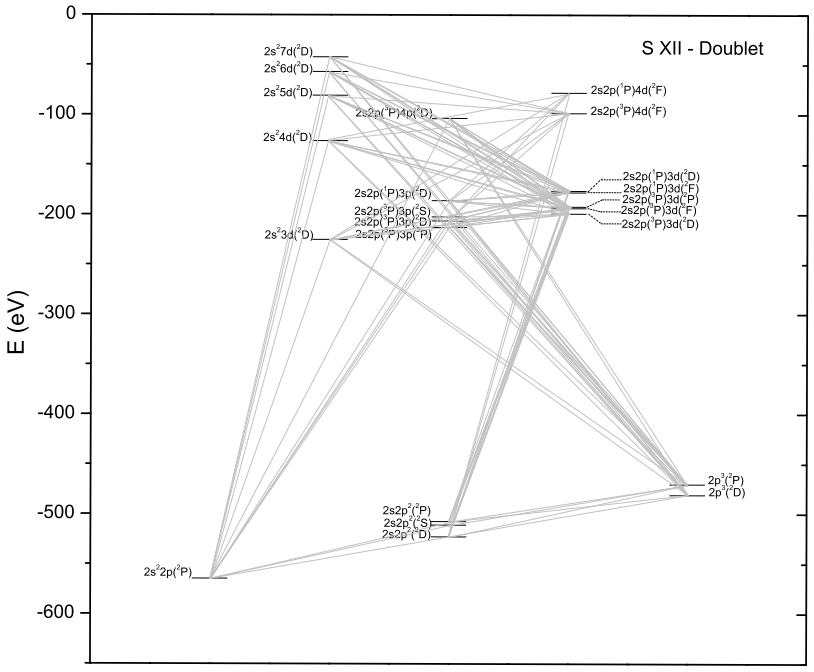

Figure 4. Grotrian diagram for the S XII doublet. The gray lines show the transitions included in our model. All data are collected from *Ralchenko et al.* [2008].

From Figures 6a and 6b we see that the spectra keep more or less the same shape as E_{init} is reduced from 2 to 1.2 MeV/u, except in the photon energy range of 500–700 eV. This drop of initial ion energy changes the CX collision number distribution of sulfur ions (there are less highly charged sulfur ions going through CX collisions) but leaves those of carbon and oxygen almost unaffected. In this way, the high-energy tail of the sulfur spectrum is reduced and results in deeper "valleys" around 400, 520, and 610 eV. When the initial ion energy is decreased to 0.6 MeV/u, the spectra change more

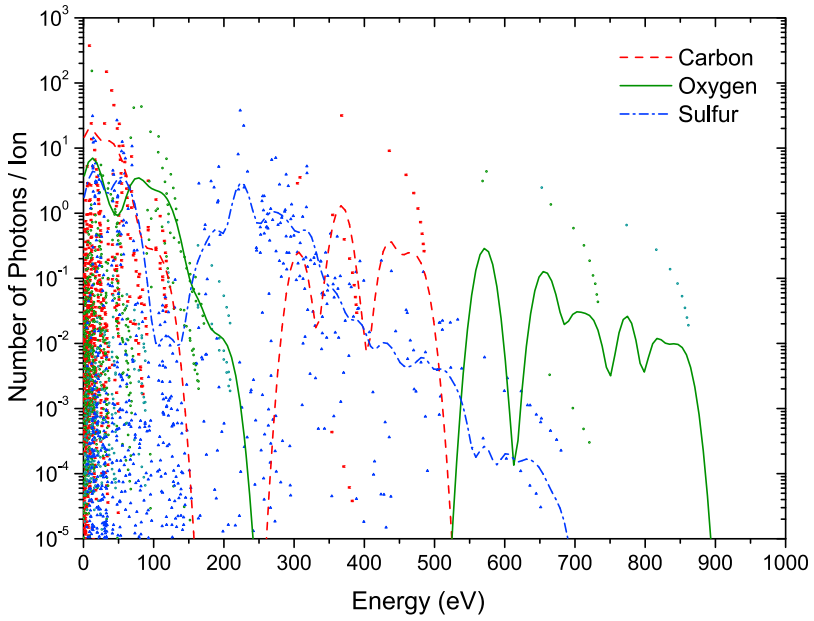

Figure 5. Emission lines and synthesized spectra for equal abundances of C, O, and S with N_{tot} = 1000, q_{init} = 1 and E_{init} = 1.2 MeV/u. Individual lines are marked with different symbols and colors (squares, red, and dashed curve for carbon; circles, green, and solid curve for oxygen; and triangles, blue, and dashed-dotted curve for sulfur). For each element the line profile is assumed to be a Gaussian with a fixed FWHM equal to 10 eV. At a given photon energy, contributions from all the Gaussian lines belonging to a single element are summed, the smooth curves showing the resultant synthetic spectra.

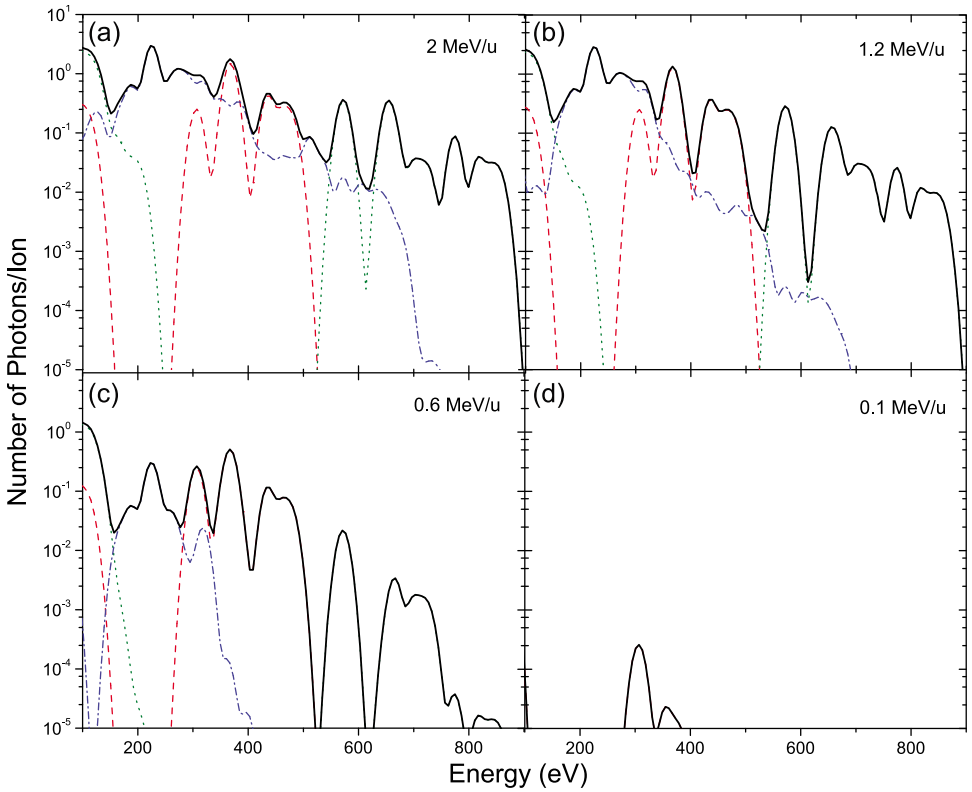

Figure 6. Synthetic spectra for varying initial ion energies. The elemental abundances are equal and q_{init} = 1. Contributions from carbon, oxygen, and sulfur are indicated by the red dashed, green dotted, and blue dashed-dotted curves, respectively. The total spectrum is given by the solid black curve.

dramatically because not only the CX collision number distribution of sulfur ions is altered significantly but also those of carbon and oxygen (see Figure 3). In this case the spectra in the range of 300–520 eV and 520–800 eV are reduced due to less carbon and oxygen emissions, respectively, and there is little photon yield beyond 800 eV. Low charge states of oxygen and sulfur ions account for the low-energy spectra (below 280 eV) where carbon emission is too weak to give a substantial contribution. The total flux is also reduced when compared to the case of high initial ion energy. At the extremely low initial ion energy of 0.1 MeV/u (shown in Figure 6d), we see that there is very little emission in this wave band from any of the three elements except the carbon feature at around 300 eV.

4. Spectral Fitting Procedure

[17] In order to provide a quantitative comparison of our synthetic spectra with the XMM-Newton and Chandra observations of the Jovian X-ray auroras we employ the standard X-ray spectrum analyzing software package Xspec (version 12.5.0) to fit the observations. Because the ion collisions and photon emission for each element are independent, the first three parameters of the fitting procedure are the initial ion energies of C, O, and S at the top of the Jovian atmosphere. We chose a grid of initial ion energies (E_{init} = 0.02, 0.04, 0.06, 0.08, 0.1, 0.2, 0.4, 0.6, 0.8, 1.0, 1.2, 1.4, 1.6, 1.8, and 2.0 MeV/u), keep N_{tot} = 1000 and q_{init} = 1 fixed, and, in order to find the model spectrum at an initial ion energy that is not on a grid point, we interpolate the relative intensity for each emission line at the given initial ion energy. The total spectrum is the sum of contributions from each element, and we introduce two more fitting parameters: the relative abundances of C and S with respect to that of oxygen, A_C and A_S, respectively. To estimate the line resolution, we include the FWHM as a free parameter. The Xspec routine "coscas" is then able to generate a synthetic spectrum by (1) interpolating to find the relative intensity at a given ion energy for a given element; (2) computing the Gaussian line profiles at the binning energies provided by the calling function in Xspec; and (3) summing up all the contributions from each element according to their relative abundances. Xspec also requires a normalization factor (NORM) for each model component in the fit. Since we calculate only the relative intensities of emission lines, the units of the model output are arbitrary and the normalization absorbs all other factors affecting the flux.

5. Spectral Fitting

[18] We report here the model fitting results for both the XMM-Newton and Chandra observations of Jupiter. For the XMM-Newton observations (OBS ID 0158760101, 0200080201, 0200080701), we fit to the processed spectra from *Branduardi-Raymont et al.* [2004, 2007a]. The Chandra observations (OBS ID 3726 and 4418) were made by *Elsner et al.* [2005] but since that time new data reduction algorithms have been recommended, so we have used

Table 1. Results of Model Fits to XMM-Newton Observations of the Jovian North and South Polar X-Ray Auroras[a]

OBS ID (Date)	E_O (MeV/u)	E_S (MeV/u)	A_S	FWHM (eV)	NORM CX Model	Γ	NORM Power Law	Red. χ^2 [DOF]
0158760101 North (4.28–29.2003)	$1.05^{+0.09}_{-0.21}$	$2.00^{+*}_{-0.60}$	$0.31^{+0.19}_{-0.17}$	3^{+11}_{-2}	$(1.8^{+1.6}_{-0.3})^{-6}$	$2.6^{+1.3}_{-3.0}$	$(3.6^{+1.8}_{-1.4})^{-6}$	1.08 [33]
0200080201 North (11.25–26.2003)	$0.97^{+0.18}_{-0.35}$	$2.00^{+*}_{-0.57}$	$0.32^{+0.20}_{-0.20}$	3^{+32}_{-2}	$(1.7^{+6.1}_{-0.7})^{-6}$	$2.2^{+0.9}_{-1.3}$	$(5.9^{+1.7}_{-1.7})^{-6}$	1.51 [35]
0200080701 North (11.27–29.2003)	$1.13^{+0.16}_{-0.17}$	$2.00^{+*}_{-0.43}$	$0.32^{+0.22}_{-0.18}$	12^{+16}_{-10}	$(1.12^{+0.74}_{-0.38})^{-6}$	$1.7^{+1.0}_{-2.1}$	$(5.4^{+1.7}_{-1.6})^{-6}$	1.26 [36]
0158760101 South (4.28–29.2003)	$1.1^{+0.2}_{-0.8}$	0.77^{+*}_{-*}	1^{+660}_{-*}	3^{+150}_{-*}	$(3.7^{+7.8}_{-2.3})^{-7}$	$2.0^{+0.5}_{-1.2}$	$(5.6^{+1.9}_{-2.4})^{-6}$	0.83 [19]
0200080201 South (11.25–26.2003)	$1.06^{+0.22}_{-0.29}$	$1.53^{+*}_{-0.30}$	$0.63^{+0.72}_{-0.43}$	3^{+26}_{-2}	$(0.8^{+1.8}_{-0.3})^{-6}$	-2.96^{+*}_{-*}	$(0.2^{+1.2}_{-0.1})^{-5}$	0.55 [28]
0200080701 South (11.27–29.2003)	$1.31^{+1.0}_{-0.41}$	0.5^{+*}_{-*}	867^{+39}_{-*}	$3^{+8.5}_{-2}$	$(3.2^{+8.5}_{-1.2})^{-7}$	$1.32^{+0.42}_{-0.61}$	$(7.6^{+2.0}_{-1.9})^{-6}$	1.03 [30]

[a]The columns give best fit initial ion energies, sulfur abundances relative to oxygen, FWHM line widths, spectrum normalization for the CX model component of the synthetic spectrum (in units of ion cm^{-2} s^{-1}), the exponent for the power law fit to the high-energy tail of the spectrum, the normalization for the power law component (in units of ph cm^{-2} s^{-1} keV^{-1}), and reduced chi square and degree of freedom (defined as the number of spectral energy bins minus the number of independent inputs) for the full synthetic spectrum (CX model and power law components). All uncertainties are computed with $\Delta\chi^2 = 2.706$, equivalent to 90% confidence for a single parameter. The asterisk in the errors means that the parameter is not bounded in that direction. The superscript outside of the bracket represents the power of 10.

several different reprocessing algorithms (to adjust the pulse height amplitudes (PHA) in the LEVEL 1 event files) to determine if they have any significant effect on the fitting. The details of the algorithms applied can be found in Appendix A. An initial analysis of the Chandra observations using our new model has recently been reported [*Hui et al.*, 2009].

5.1. XMM-Newton Data and Fits

[19] The previously reduced XMM-Newton spectra and their response files [*Branduardi-Raymont et al.*, 2004, 2007a] are used for our fits. The fitting approach taken by *Branduardi-Raymont et al.* [2004, 2007a] was to use a combination of independent Gaussian lines which was applied to fit the various emission lines in the spectra. They also used a power law to account for the X-ray emission harder than 1 keV. Even though we focus here on the soft X-ray emission between 0.3 and 1 keV, we have included this power law (NORM $\times$ $\mathcal{E}^{-\Gamma}$, where $\mathcal{E}$ is the photon energy and NORM and Γ are adjustable parameters) in our fitting procedure for consistency.

[20] It turns out that the best fit of the spectra require initial carbon ion energies (E_C) below 0.1 MeV/u and the relative abundance of carbon to oxygen (A_C) is usually unbound, implying that carbon is not needed in the fit. This is very similar to the fits to the Chandra data recently reported [*Hui et al.*, 2009] and described below. To make an additional comparison of the contributions from carbon and sulfur, we also fit the observed spectra with two models: one including only carbon and oxygen, with the C/O ratio fixed to 0.5265 [*Schwadron and Cravens*, 2000] typical of the solar wind, and the other with only sulfur and oxygen. We find that the sulfur-oxygen model fits the data better than the carbon-oxygen model does, with one exception for OBS 0200080201 (both north and south) where the reduced χ^2 improves after switching to the carbon-oxygen model. With the lack of a prominent spectral feature in the 425 to 475 eV range expected from carbon ions, these analyses lead us to exclude carbon in the following fits by setting its relative abundance to zero.

[21] The fitting results for the power law plus our synthetic spectral model are shown in Table 1, and the observations and synthetic spectra are shown in Figure 7 and Figure 8. Table 1 lists the best fit values of the oxygen and sulfur ion energies, the relative abundance of sulfur, the line width FWHM, the normalization for the CX model component, the power law index Γ, the normalization for the power law component, and the reduced chi-square and degree of freedom (DOF, a measure of the signal to noise ratio of the fitted spectrum). We also display the fitting results for E_O, E_S, and A_S in Figure 9, comparing the results for different observations in a graphical form.

[22] Without carbon, we see from Figures 7 and 8 that the fit to the observations is quite reasonable, confirmed by the χ^2 values shown in the table. However the observed south polar spectra have greater noise and poorer statistics so some of the fitted parameters are less well constrained than for the north polar observations. For example, fits to the northern observations yield most favored initial oxygen ion energies of approximately 1 MeV/u and sulfur ion energies of 1.5 to 2 MeV/u or higher with reasonable consistency, as illustrated particularly in Figure 9. In contrast, fits to the southern observations confirm the favoring of oxygen energies of around 1 MeV/u but with less consistency and have a much wider spread of favored sulfur energies ranging from about 0.5 to 1.5 MeV/u. Similarly, the fits to the north polar observations consistently yield relative sulfur abundances of about 0.3 (meaning that there is about one sulfur ion for every three oxygen ions) whereas for the south polar observations the value is bounded reasonably only for one of the three observations, for which $A_S \sim 0.6$. Owing to the small number of observed X rays in the high-energy tail of the spectrum, not surprisingly, the best fit values of the power law constant Γ show wide variations as well. Without the outlying value of -2.96 for OBS 0200080201, the others range from about 1.5 to 2.5. The line width parameter is consistently found to be about 3 eV across all the observations except one, which is much smaller than the energy resolution of the CCDs used by XMM-Newton.

5.2. Chandra Data and Fits

[23] As with the fits to the XMM-Newton observations, our analysis for the Chandra spectra indicates that the best fits are obtained without carbon ions as we initially reported recently [*Hui et al.*, 2009]. This is especially obvious when we performed the comparative fits using the carbon-oxygen and sulfur-oxygen models. For all Chandra observations considered here, the reduced χ^2 is significantly better for the sulfur-oxygen model compared to the carbon-oxygen model. We therefore eliminate carbon from the ion sources in the following fits.

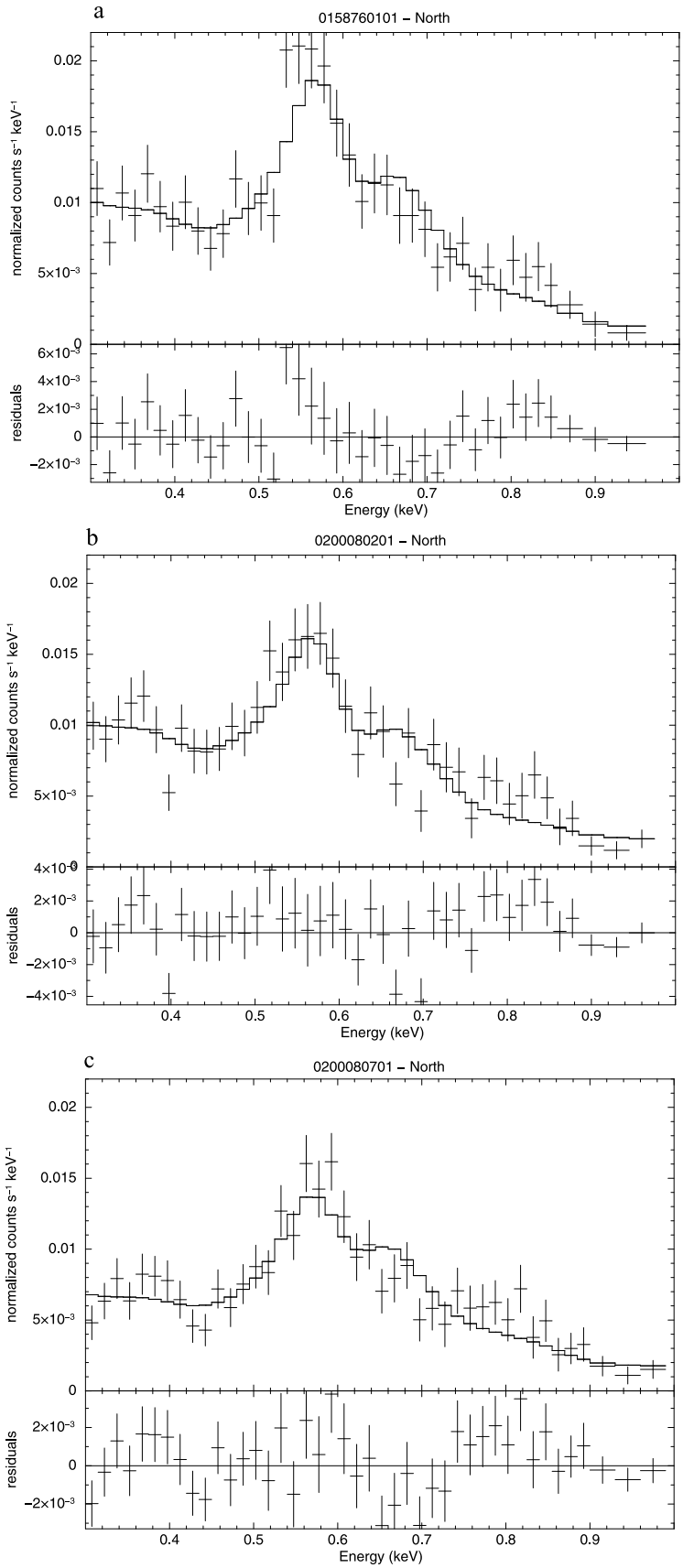

Figure 7. Model fits to the north polar spectra observed by XMM-Newton.

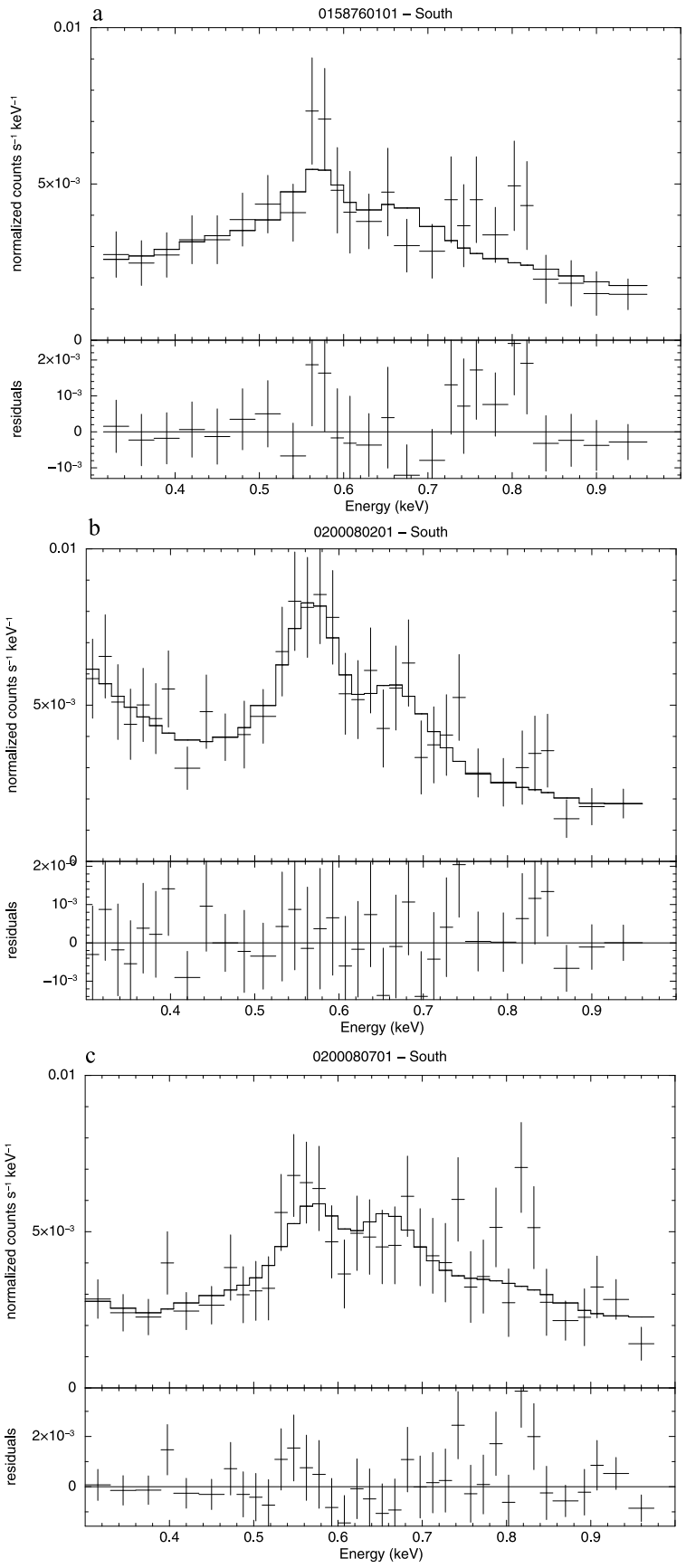

Figure 8. Model fits to the south polar spectra observed by XMM-Newton.

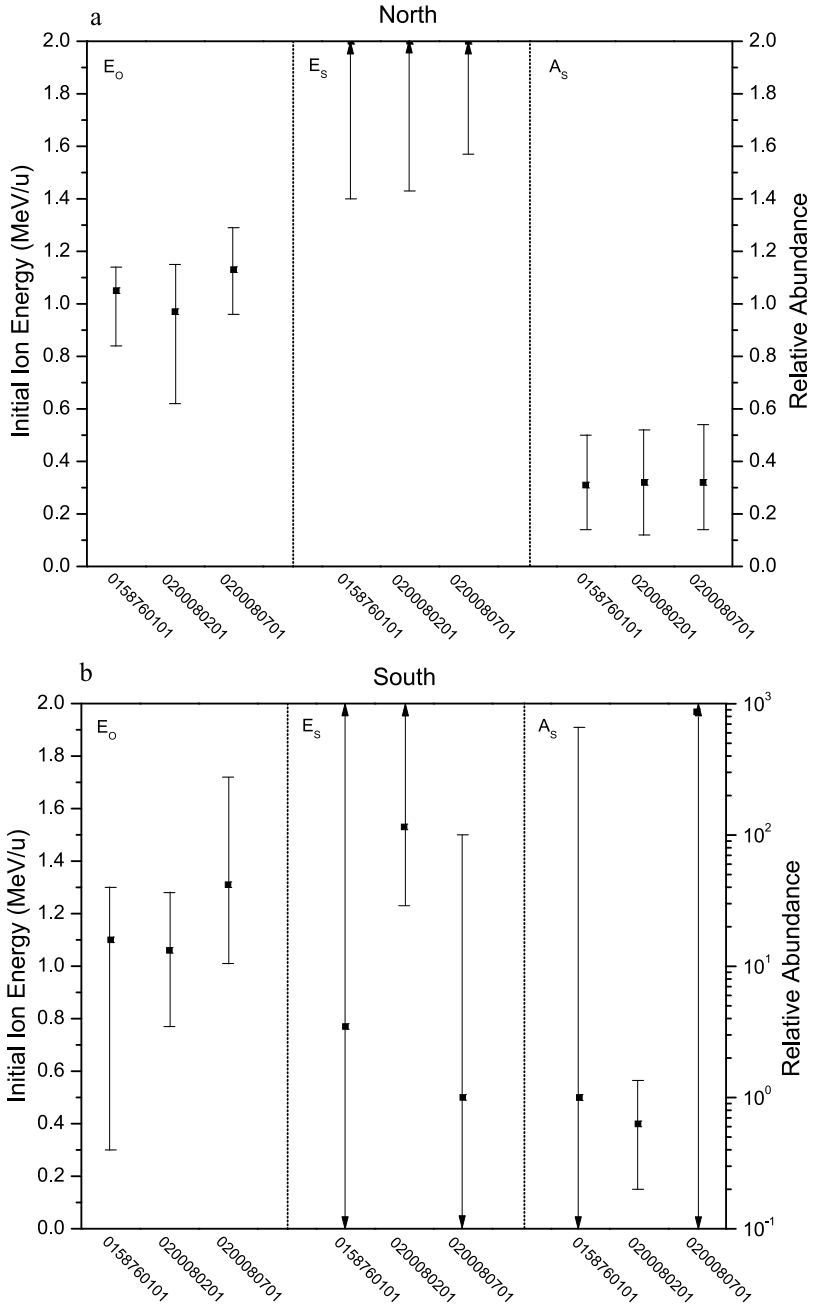

Figure 9. Illustration of the fitting results for the XMM-Newton observations. The best-fit values are shown by symbols and the uncertainties are computed with $\Delta\chi^2 = 2.706$, equivalent to 90% confidence for a single parameter. An arrow in the graph indicates that the parameter is not bounded in that direction. Results for the three observations (ID 0158760101, 0200080201, and 0200080701) are shown for the inferred initial ion energies (E_O and E_S, left-hand scale) and relative abundance of sulfur to oxygen (A_S, right-hand scale).

[24] Without carbon in the fitting procedure, we display the results at the 90% confidence level in Table 2 and show the corresponding synthetic spectra in Figures 10 and 11. As with the fits for the XMM-Newton observations, we also illustrate the best fit values of E_O, E_S, and A_S and their uncertainties graphically in Figure 12. Table 2 and Figures 10–12 include not only results for the north and south poles but also three new processings of the raw observation data, Adj01, Adj02, and Adj03 (see Appendix A) that have been developed since the observations, along with those for the original processing of *Elsner et al.* [2005] labeled "E2005." Since the initial fits we made always yielded FWHM values close to 55 eV, we fixed this value for the subsequent calculations to speed up the fitting procedure. Also as with the fits to the XMM-Newton observations, the χ^2 values indicate that the fits are statistically quite reasonable.

[25] Immediately apparent from Table 2 is the fact that the various processings of the raw data do not have a significant

Table 2. Results of Model Fits to Chandra Observations of the Jovian North and South Polar X-Ray Auroras[a]

OBS ID (Date)	Data Reduction	E_O (MeV/u)	E_S (MeV/u)	A_S	NORM	Reduced χ^2 [DOF]
3726 North (2.24–25.2003)	Adj01	$1.30^{+0.28}_{-0.16}$	$0.56^{+0.12}_{-0.12}$	63^{+233}_{-32}	$(1.32^{+0.67}_{-0.41})^{-6}$	0.64 [15]
	Adj02	$1.20^{+0.21}_{-0.12}$	$0.51^{+0.02}_{-0.02}$	204^{+154}_{-202}	$(1.51^{+0.89}_{-0.48})^{-6}$	1.06 [12]
	Adj03	$1.48^{+*}_{-0.28}$	$0.81^{+0.48}_{-0.45}$	5^{+243}_{-3}	$(1.06^{+0.52}_{-0.32})^{-6}$	0.64 [13]
	E2005	$1.24^{+0.29}_{-0.23}$	$0.78^{+0.09}_{-0.22}$	3^{+17}_{-1}	$(1.4^{+1.1}_{-0.5})^{-6}$	1.13 [14]
3726 South (2.24–25.2003)	Adj01	$2.00^{+*}_{-0.80}$	$2.00^{+*}_{-0.84}$	$0.8^{+1.1}_{-0.4}$	$(3.4^{+5.3}_{-0.7})^{-7}$	0.96 [5]
	Adj02	$2.00^{+*}_{-0.70}$	$1.86^{+*}_{-0.33}$	$0.94^{+0.78}_{-0.44}$	$(3.4^{+2.2}_{-0.7})^{-7}$	1.05 [6]
	Adj03	$2.00^{+*}_{-0.66}$	$1.52^{+*}_{-0.81}$	$1.5^{+4.3}_{-1.0}$	$(3.3^{+4.4}_{-0.8})^{-7}$	1.29 [6]
	E2005	$2.00^{+*}_{-0.58}$	$1.44^{+*}_{-0.71}$	$1.1^{+2.0}_{-0.5}$	$(3.7^{+2.1}_{-0.8})^{-7}$	0.87 [6]
4418 North (2.25–26.2003)	Adj03	$2.00^{+*}_{-0.37}$	$0.98^{+0.26}_{-0.42}$	$2.5^{+2.6}_{-1.3}$	$(7.3^{+1.2}_{-0.8})^{-7}$	1.05 [19]
4418 South (2.25–26.2003)	Adj03	$2.00^{+*}_{-0.47}$	$0.68^{+0.64}_{-0.24}$	17^{+94}_{-16}	$(4.2^{+1.0}_{-0.6})^{-7}$	1.43 [11]

[a]Four processings of the raw observation data are given for OBS 3726 as described in the text and Appendix A. The columns give best fit initial ion energies, sulfur abundances relative to oxygen, spectrum normalization (in units of ion cm^{-2} s^{-1}), reduced chi square and degree of freedom (defined as the number of spectral energy bins minus the number of independent inputs). The FWHM is fixed at a value of 55 eV for all fit results displayed. All uncertainties are computed with $\Delta\chi^2 = 2.706$, equivalent to 90% confidence for a single parameter. The asterisk in the errors means that the parameter is not bounded in that direction. The superscript outside of the bracket represents the power of 10.

effect on the best fit values of the model's parameters. However, examination of Figures 10 and 11 shows that even though the fits are quite similar for the four processings of the raw event files, significant localized differences in the spectra result from the different processing. For example, for the OBS 3726 north polar spectrum, the original processing displays a very strong and narrow peak at about 680 eV, whereas this peak is much smaller, broader, or even a dip in the other processings.

[26] We also note that generally the fits to the north polar spectra constrain the initial ion energies better than those of the south polar aurora, shown by relatively smaller uncertainty ranges of the fit parameters. This can be understood given the fact that the north polar spectra have better signal-to-noise (judging from their larger DOF) than those for the south polar region. Therefore, perhaps surprisingly, the relative abundance of sulfur for the south polar fits have much lower uncertainties of the fit values than for the north polar fits. This apparent contradiction is resolved once one notices that the south polar fits generally predict larger values of E_S but, from our discussion of how the synthetic spectrum changes with varying initial ion energy, we know that the lower E_{init}, the less the contribution of that ion to the total spectrum for fixed ion abundance. Therefore to account for a certain spectral feature needing the contribution of a specific ion, the model has to increase the abundance of that ion in order to create the same amount of emission when the initial ion energy is forced to lower values in the fitting process.

[27] Table 2 and Figure 12 show that the most favored value of E_O is between 1 and 2 MeV/u for the northern spectra and 1.5 to 2 MeV/u or higher for the southern spectra generally in agreement with the fit results for XMM-Newton which favored about 1 MeV/u for the northern and southern spectra. The fits for Chandra observations of the north polar spectra yield best fits for E_S between 0.5 and 1 MeV/u and 0.5 to 2 MeV/u or higher for the south polar spectra, whereas the XMM-Newton results favor 1.5 to 2 MeV/u for the north and 0.5 to 1.5 MeV/u for the south. The relative abundance of sulfur with respect to oxygen for the fits to the Chandra observations similarly show significant variation between north and south, between observations, and with those from XMM-Newton. Specifically, the Chandra best fit A_S is about 3 or higher for the north polar spectra (compared to about 0.3 for XMM-Newton) and about 1.5 or higher for the south polar spectra (compared to about 0.6 with large uncertainty for XMM-Newton).

6. Discussion

[28] *Branduardi-Raymont et al.* [2007a] found, by combining all the XMM-Newton spectra, that sulfur emissions are more likely than those from carbon, but better quality data were needed to reach a definite conclusion. Through the present charge exchange induced X-ray emission model fits to the XMM-Newton observations, we find carbon's contribution is generally less significant to the detected emissions than that from sulfur (from the C-O/S-O model comparison), leading us to consider the overall spectral analysis in favor of the magnetospheric ion origin because of the strong lack of carbon required in the "C, S, and O" model fit. However, this kind of "mixture" of magnetospheric and solar wind origins might suggest a possible reason for the temporal variation of the ion sources.

[29] This also agrees with our initial modeling of the Chandra observations [*Hui et al.*, 2009] which has been extended here. Therefore we infer that the ions that are accelerated to high energy and precipitate into the Jovian atmosphere resulting in X-ray emission are likely of magnetospheric rather than solar wind origin. That is, if the solar wind played an important role as a source of these ions, then carbon should be required in the model because, after oxygen, it is the next most abundant component of the solar wind that leads to X-ray emission. Otherwise, a mechanism of acceleration of oxygen ions but not carbon ions would have to exist. As pointed out by *Hui et al.* [2009], other observations detecting X rays from comets show clear identification of C and O emission and are definitely of solar wind origin [*Kharchenko and Dalgarno*, 2000; *Lisse et al.*, 2001; *Cravens*, 2002; *Krasnopolsky et al.*, 2004]. In contrast, at Jupiter, a mechanism must exist that accelerates magnetospheric oxygen and sulfur ions to above 1 MeV/u before precipitation into the upper atmosphere.

[30] From the present analysis, it is also clearly the case that the Jovian polar X-ray emission is significantly variable in space (north versus south polar aurora) and time (observation date). That is, we find significant variation needed to fit the individual observations of the north and south polar ion precipitations. In addition, we find a wide variation in initial ion energies and abundances for the various existing

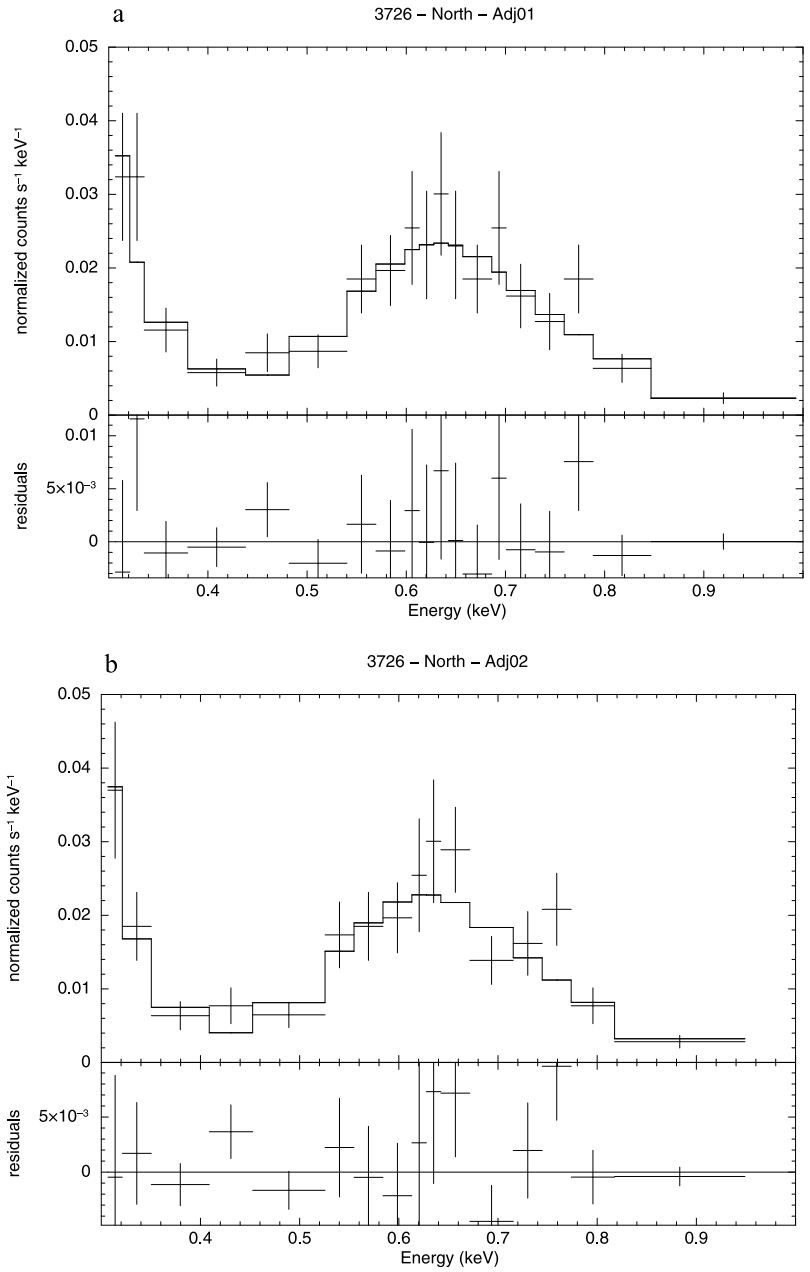

Figure 10. Model fits to the spectra of the north polar X-ray aurora observed by *Chandra* (OBS ID 3726). Shown are three different data reduction methods (denoted as Adj01, Adj02, and Adj03, see Appendix A) applied to the observation and the original spectra processed by *Elsner et al.* [2005].

observations. The time scale of this variation is likely to be relatively short since the Chandra observations took place in February 2003 and the first of the XMM-Newton observations took place in April 2003 and yet rather different initial ion characteristics are needed to fit the spectra. The same can be said of the second and third XMM-Newton observations which took place even closer in time, namely on 25–26 November 2003 and 27–29 November 2003. Clearly, additional observations are needed to constrain the range of this variability and its period (or periods) to enable deeper understanding of the ion source (or sources) and acceleration mechanism [e.g., *Gladstone et al.*, 2002]. For example, is the time variability associated with orbital periods of the Galilean satellites or interactions of the solar wind with the Jovian magnetosphere?

[31] If we consider only the Chandra observations, then the favored values of E_O are about twice that of E_S, in reasonable accord with the assumption that the initial ions are mainly singly charged, as pointed out by *Hui et al.* [2009], because of the likely ion acceleration mechanism described by *Cravens et al.* [2003] and *Bunce et al.* [2004]. However, the present fits to the XMM-Newton observations suggest that these initial energies are more nearly equal or that E_S might be significantly greater than E_O. Even taking into account a typical ±10% cross-calibration discrepancy between the two observatories [*Plucinsky et al.*, 2008], this

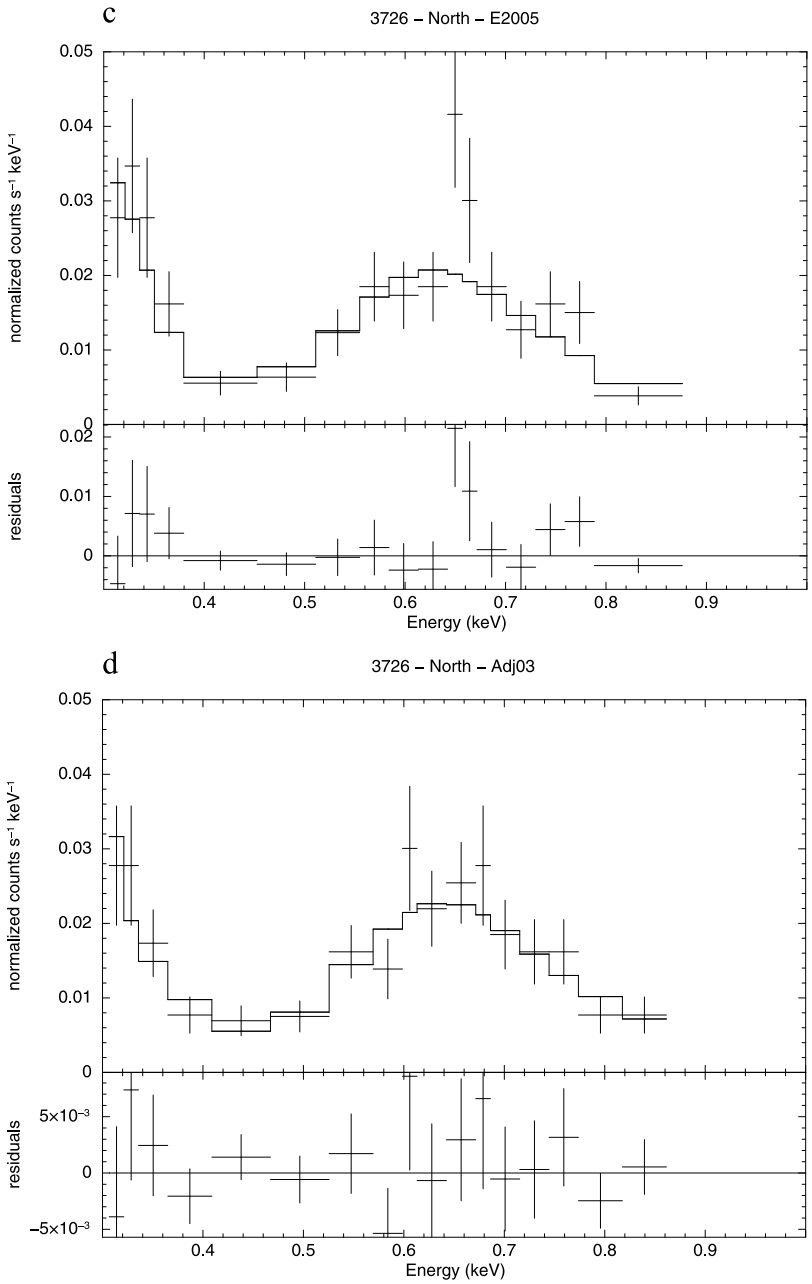

Figure 10. (continued)

still indicates the significant variability of the spectra and the possible seeding ion characteristics. Similarly, while fits to the Chandra spectra favor a greater abundance of sulfur over that of oxygen (i.e., $A_S > 1$), analysis of the XMM-Newton spectra favor $A_S \leq 1$. In fact, the difference in the inferred relative sulfur abundance corresponds to the larger E_S required in the XMM-Newton fits. Because the sulfur ions account for the majority of the low-energy X-ray spectra (200–400 eV) and this part of the spectra is distorted more severely in the reduction of the Chandra observations than in the case of XMM-Newton, we expect that the XMM-Newton fits would provide a better inference of the energy and abundance of sulfur ions. This further underscores the need for new observations with better signal to noise and, ultimately, greater resolution in order to improve our understanding of the ion characteristics and the acceleration mechanism.

[32] Finally, we note that in our previous study of the Chandra observations [*Kharchenko et al.*, 2008], we discussed a possible quenching effect on the spectra due to collisions between metastable O^{6+} ions and atmospheric gas molecules. This effect may explain the suppression of the $2^3S \rightarrow 1^1S$ transitions of O^{6+} at 561 eV which are diminished in the Chandra spectra. However, in the XMM-Newton spectra, and the model fits presented here, the O^{6+} 561 eV line is one of the dominant features in all spectra for both north and south polar auroras. This difference between the Chandra and XMM-Newton observations has several

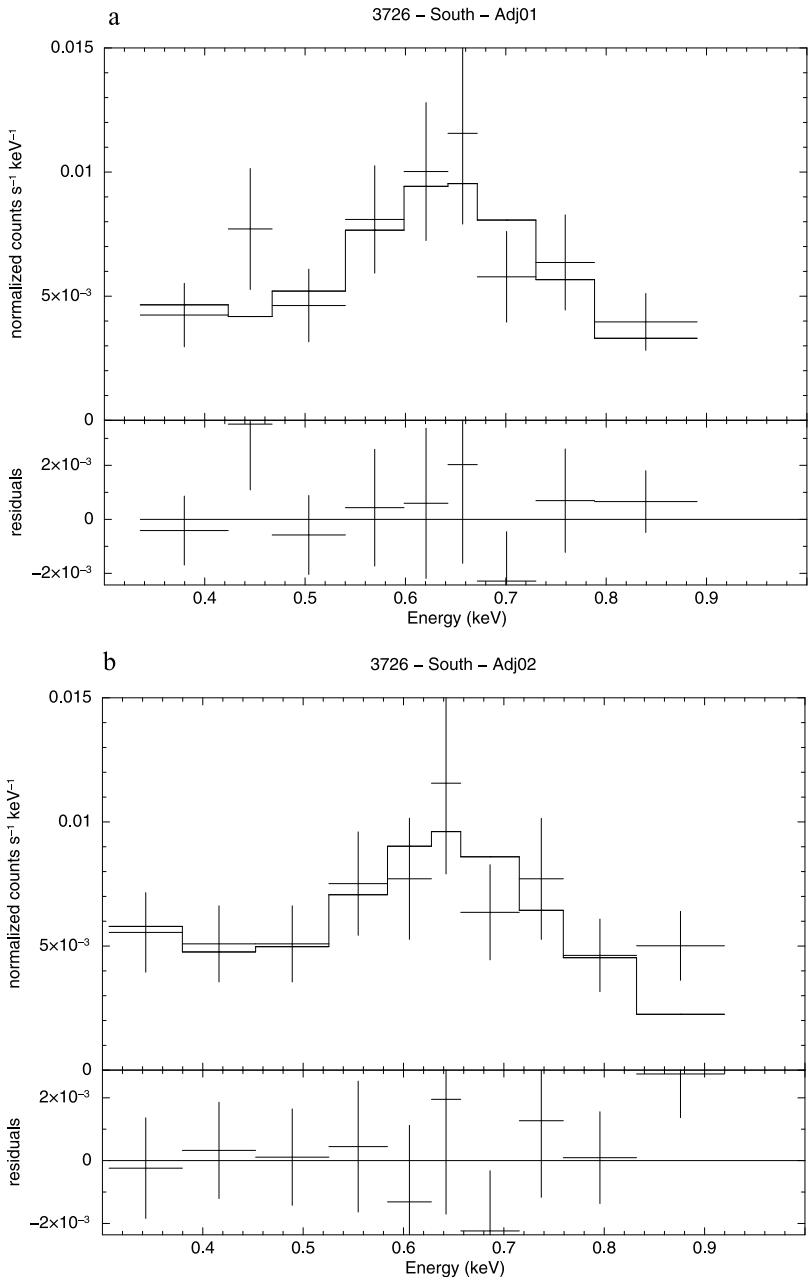

Figure 11. Model fits to the spectra of the south polar X-ray aurora observed by *Chandra* (OBS ID 3726). Shown are three different data reduction methods (denoted as Adj01, Adj02, and Adj03, see Appendix A) applied to the observation and the original spectra processed by *Elsner et al.* [2005].

implications. First, the quenching effect, which depletes the O^{6+} 2^3S population before it can radiate and whose efficiency will increase with depth into the Jovian atmosphere, may be quite variable in the time spans between the Chandra and XMM-Newton observations. Second, the suppression of the 561 eV feature may result partially from the relatively low energy resolution of the Chandra spectra. This quenching effect, as suggested by *Kharchenko et al.* [2008], could be used as a probe of the depth of penetration of the precipitating ions. To quantify the efficiency of the quenching effect and its role in the Jovian X-ray aurora emission and to provide an understanding of the differences between the XMM-Newton and Chandra spectra will require future observations at higher sensitivity.

[33] In summary, the present work has compared model fits for both Chandra and XMM-Newton observations of the Jovian polar aurora, demonstrating from the inferred precipitating ion energies and relative abundances for each spectral observation that they are significantly variable in time (observation date) and space (north and south polar X-ray aurora). The work has also extended our preliminary analysis of only the Chandra spectra [*Hui et al.*, 2009], which used a new synthetic spectra model described here in detail, that showed the relatively unimportance of including carbon in

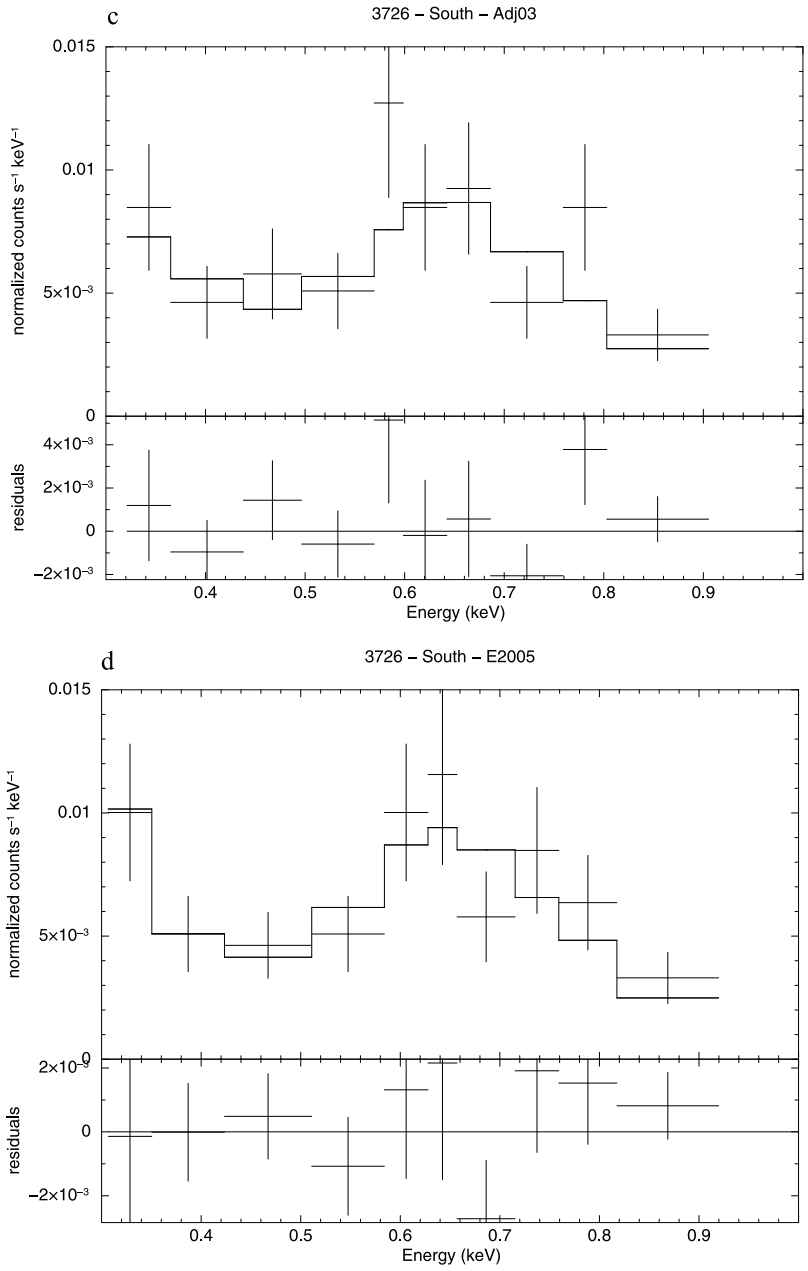

Figure 11. (continued)

the model implying a magnetospheric origin for the ion precipitation rather than from the solar wind.

Appendix A: Reprocessing of Chandra Event Files

[34] The data reduction of the Chandra observations ID 3726 and 4418 requires four steps: (1) make proper adjustment to the PHA values in order to reconstruct a meaningful event island for observations of optically bright objects such as Jupiter; (2) reprocess the PHA-adjusted event file (LEVEL 1) with acis_process_events to obtain the LEVEL 2 event file; (3) reconstruct the coordinates of events by using proper ephemeris files so that photons are reprojected to the center of Jupiter; and (4) extract the spectrum and its corresponding response files (RMF and ARF) by applying the latest calibration. Because steps 2 to 4 are standard processing procedures and well documented on the Web site of CIAO, the data analysis software package for Chandra, here we describe only the first step of the new data reduction.

[35] To begin with, the original LEVEL 1 event files are modified by adjusting the PHA values with three different algorithms. The purpose of this adjustment is to evaluate the background and bias and make corresponding corrections. In the TIMED VFAINT mode which was used in observations 3726 and 4418, PHAs are recorded in a 5 × 5 pixel

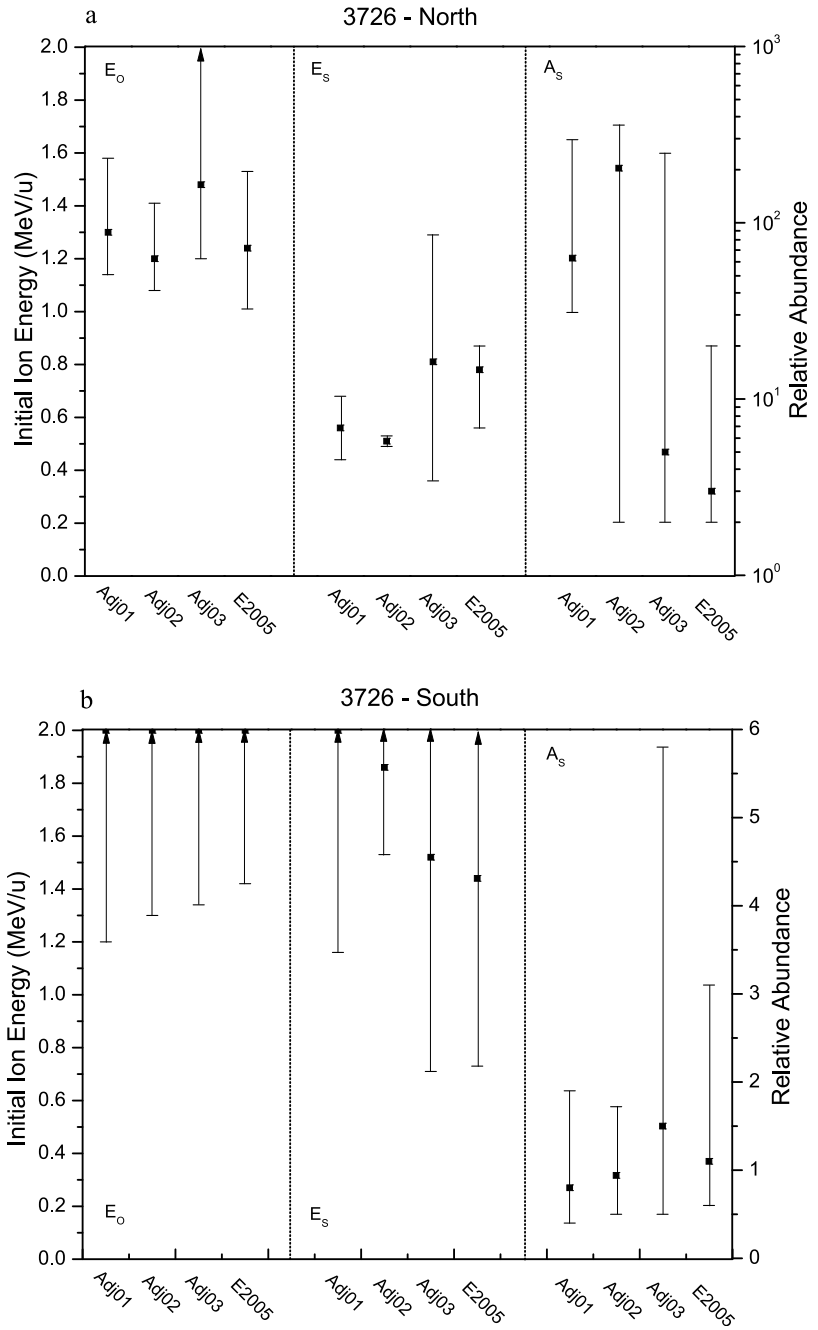

Figure 12. Illustration of the fitting results of the Chandra observation (ID 3726). The best-fit values are marked by symbols and the uncertainties are computed with $\Delta\chi^2 = 2.706$, equivalent to 90% confidence for a single parameter. An arrow in the graph indicates that the parameter is not bounded in that direction. Results from three different data reduction methods (denoted as Adj01, Adj02, and Adj03, see Appendix A) and that from the original spectra processed by *Elsner et al.* [2005] are shown for the inferred initial ion energies (E_O and E_S, left-hand scale) and relative abundance of sulfur to oxygen (A_S, right-hand scale).

event island (instead of just a 3 × 3 event island in the FAINT mode) centered on each event. Among the total 25 pixels, only the nine pixels in the center of the 5 × 5 pixel event island (shown by black circles in Figure A1) are used to compute the total PHA. The outer 16 pixels (denoted by red squares in Figure A1) are additional information that can be used to examine the background and bias, and the three algorithms differ in how to use this additional information.

[36] The first algorithm (Adj01) estimates the amount of PHA adjustment by taking the median of the pixels around the edge of the 5 × 5 pixel event island. Owing to the effects of charge-transfer inefficiency (CTI), however, some of the

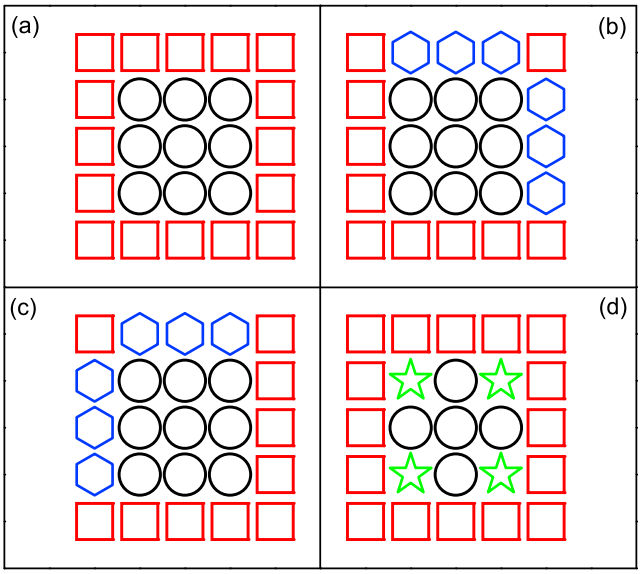

Figure A1. Illustration of the 5 × 5 pixel event island used in the TIMED VFAINT mode of Chandra observations 3726 and 4418 (see Appendix A). Different selection patterns of the pixels used in the PHA adjustment algorithms are shown by different color combinations. Pattern a is used in Adj01, patterns b and c are used in Adj02, and pattern d is used in Adj03.

pixels are excluded. For an event that is recorded on the first or third quadrants of the 5 × 5 pixel event island, the pixels marked with blue hexagons in Figure A1b are removed from the calculation. Similarly, for an event that hits on the second or fourth quadrants, the pixels marked with blue squares in Figure A1c are excluded in the calculation.

[37] The second algorithm (Adj02) uses the median of the smallest 16 of the 25 PHAs as the adjustment. There is no limit in Adj02, unlike in Adj01, on which PHAs can be included in the calculation. This algorithm is either very similar or identical to the one used in *Elsner et al.* [2005], depending on whether the mean or the median of the smallest 16 of 25 PHAs was used. The differences between the extracted spectra of Adj02 and E2005 (see Figures 10 and 11) can be attributed to this uncertainty of PHA adjustment and the different calibrations applied in the spectral extractions.

[38] The last algorithm (Adj03) takes the median of the four corner pixels (marked with green stars in Figure A1d) as the PHA adjustment. This algorithm may result in more uncertainty than the other two because the PHA adjustment is based on the smallest number of pixels and the corner pixels may contain charge associated with a legitimate X-ray event. However, we find no significant difference between the final spectra of Adj03 and those from Adj01, Adj02, and E2005.

[39] **Acknowledgments.** This work has been supported by NASA Planetary Atmospheres Program grant NNH07AF12I. We are grateful to the Chandra Helpdesk staff, particularly Elizabeth Galle, for assistance with processing the raw observations files. We also acknowledge Glenn E. Allen who coded the new Chandra data reduction algorithms.

[40] Wolfgang Baumjohann thanks Ronald Elsner and another reviewer for their assistance in evaluating this paper.

References

Bhardwaj, A., and G. R. Gladstone (2000), Auroral emissions of the giant planets, *Rev. Geophys.*, *38*, 295, doi:10.1029/1998RG000046.

Bhardwaj, A., et al. (2005), Solar control on Jupiter's equatorial X-ray emissions: 26–29 November 2003 XMM-Newton observation, *Geophys. Res. Lett.*, *32*, L03S08, doi:10.1029/2004GL021497.

Bhardwaj, A., et al. (2006), Low- to middle-latitude X-ray emission from Jupiter, *J. Geophys. Res.*, *111*, A11225, doi:10.1029/2006JA011792.

Branduardi-Raymont, G., et al. (2004), First observation of Jupiter by XMM-Newton, *Astron. Astrophys.*, *424*, 331, doi:10.1051/0004-6361:20041149.

Branduardi-Raymont, G., et al. (2007), A study of Jupiter's aurorae with XMM-Newton, *Astron. Astrophys.*, *463*, 761, doi:10.1051/0004-6361:20066406.

Branduardi-Raymont, G., et al. (2007), Latest results on Jovian disk X-rays from XMM-Newton, *Planet. Space Sci.*, *55*, 1126, doi:10.1016/j.pss.2006.11.017.

Branduardi-Raymont, G., et al. (2008), Spectral morphology of the X-ray emission from Jupiter's aurorae, *J. Geophys. Res.*, *113*, A02202, doi:10.1029/2007JA012600.

Bunce, E. J., S. W. H. Cowley, and T. K. Yeoman (2004), Jovian cusp processes: Implications for the polar aurora, *J. Geophys. Res.*, *109*, A09S13, doi:10.1029/2003JA010280.

Cravens, T. E. (2002), X-ray emission from comets, *Science*, *296*, 1042, doi:10.1126/science.1070001.

Cravens, T. E., E. Howell, J. H. Waite Jr., and G. R. Gladstone (1995), Auroral oxygen precipitation at Jupiter, *J. Geophys. Res.*, *100*, 17,153, doi:10.1029/95JA00970.

Cravens, T. E., et al. (2003), Implications of Jovian X-ray emission for magnetosphere-ionosphere coupling, *J. Geophys. Res.*, *108*(A12), 1465, doi:10.1029/2003JA010050.

Cravens, T. E., et al. (2006), X-ray emission from the outer planets: Albedo for scattering and fluorescence of solar X rays, *J. Geophys. Res.*, *111*, A07308, doi:10.1029/2005JA011413.

Elsner, R. F., et al. (2005), Simultaneous Chandra X ray, Hubble Space Telescope ultraviolet, and Ulysses radio observations of Jupiter's aurora, *J. Geophys. Res.*, *110*, A01207, doi:10.1029/2004JA010717.

Gladstone, G. R., J. H. Waite Jr., and W. S. Lewis (1998), Secular and local time dependence of Jovian X ray emissions, *J. Geophys. Res.*, *103*, 20,083, doi:10.1029/98JE00737.

Gladstone, G. R., et al. (2002), A pulsating auroral X-ray hot spot on Jupiter, *Nature*, *415*, 1000.

Horanyi, M., T. E. Cravens, and J. H. Waite Jr. (1988), The precipitation of energetic heavy ions into the upper atmosphere of Jupiter, *J. Geophys. Res.*, *93*, 7251, doi:10.1029/JA093iA07p07251.

Hui, Y.-W., D. R. Schultz, V. Kharchenko, P. C. Stancil, T. E. Cravens, C. M. Lisse, and A. Dalgarno (2009), The ion-induced charge-exchange X-ray emission of the Jovian auroras: Magnetospheric or solar wind origin?, *Astrophys. J.*, *702*, L158, doi:10.1088/0004-637X/702/2/L158.

Johnson, W. R., I. M. Savukov, U. I. Safronova, and A. Dalgarno (2002), E1 transitions between states with n = 1–6 in helium-like carbon, nitrogen, oxygen, neon, silicon, and argon, *Astrophys. J. (Supp.)*, *141*, 543, doi:10.1086/340547.

Kharchenko, V., and A. Dalgarno (2000), Spectra of cometary X-rays induced by solar wind ions, *J. Geophys. Res.*, *105*, 18,351, doi:10.1029/1999JA000203.

Kharchenko, V., W. Liu, and A. Dalgarno (1998), X ray and EUV emission spectra of oxygen ions precipitating into the Jovian atmosphere, *J. Geophys. Res.*, *103*, 26,687, doi:10.1029/98JA02395.

Kharchenko, V., A. Dalgarno, D. R. Schultz, and P. C. Stancil (2006), Ion emission spectra in the Jovian X-ray aurora, *Geophys. Res. Lett.*, *33*, L11105, doi:10.1029/2006GL026039.

Kharchenko, V., A. Bhardwaj, A. Dalgarno, D. R. Schultz, and P. C. Stancil (2008), Modeling spectra of the north and south Jovian X-ray auroras, *J. Geophys. Res.*, *113*, A08229, doi:10.1029/2008JA013062.

Krasnopolsky, V. A., J. B. Greenwood, and P. C. Stancil (2004), X-ray and extreme ultraviolet emissions from comets, *Space Sci. Rev.*, *113*, 271, doi:10.1023/B:SPAC.0000046754.75560.80.

Kingston, A. E., P. H. Norrington, and A. W. Boone (2002), Spontaneous transition rates for electric dipole (E1), magnetic dipole (M1), electric quadrupole (E2) and magnetic quadrupole (M2) transitions for He-like calcium and sulfur ions, *J. Phys. B.*, *35*, 4077, doi:10.1088/0953-4075/35/19/311.

Lisse, C. M., et al. (2001), Charge exchange-induced X-ray emission from Comet C/1999 S4 (LINEAR), *Science*, *292*, 1343, doi:10.1126/science.292.5520.1343.

Liu, W., and D. R. Schultz (1999), Jovian X-ray aurora and energetic oxygen ion precipitation, *Astrophys. J.*, *526*, 538, doi:10.1086/307994.

Maurellis, A. N., T. E. Cravens, G. R. Gladstone, J. H. Waite, and L. W. Acton (2000), Jovian X-ray emission from solar X-ray scattering, *Geophys. Res. Lett.*, *27*, 1339, doi:10.1029/1999GL010723.

Metzger, A. E., et al. (1983), The detection of X rays from Jupiter, *J. Geophys. Res.*, *88*, 7731, doi:10.1029/JA088iA10p07731.

Nahar, S. N. (2002), Relativistic fine structure oscillator strengths for Li-like ions: C IV - Si XII, S XIV, Ar XVI, Ca XVIII, Ti XX, Cr XXII, and Ni XXVI, *Astron. Astrophys.*, *389*, 716, doi:10.1051/0004-6361:20020675.

Plucinsky, P., et al. (2008), The SMC SNR 1E0102.2-7219 as a calibration standard for x-ray astronomy in the 0.3–2.5 keV bandpass, *SPIE J.*, *7011*, 68, doi:10.1117/12.789191.

Schultz, D. R., et al. (2009), *Atomic Data and Nuclear Data Tables*, in prep.

Schwadron, N. A., and T. E. Cravens (2000), Implications of solar wind composition for cometary X-rays, *Astrophys. J.*, *544*, 558, doi:10.1086/317176.

Waite, J. H., Jr., et al. (1994), ROSAT observations of the Jupiter aurora, *J. Geophys. Res.*, *99*, 14,799, doi:10.1029/94JA01005.

A. Bhardwaj, Space Physics Laboratory, Vikram Sarabhai Space Center, Trivandrum 695022, India. (anil_bhardwaj@vssc.gov.in)

G. Branduardi-Raymont, Mullard Space Science Laboratory, University College London, Holmbury St Mary, Dorking, Surrey RH5 6NT, UK. (gbr@mssl.ucl.ac.uk)

T. E. Cravens, Department of Physics and Astronomy, University of Kansas, 1251 Wescoe Hall Drive, Lawrence, KS 66045, USA. (cravens@ku.edu)

A. Dalgarno, Harvard-Smithsonian Center for Astrophysics, ITAMP, 60 Garden Street, Cambridge, MA 02138, USA. (adalgarno@cfa.harvard.edu)

Y. Hui and D. R. Schultz, Physics Division, Oak Ridge National Laboratory, Building 6010, Oak Ridge, TN 37831, USA. (huiy@ornl.gov; schultzd@ornl.gov)

V. A. Kharchenko, Physics Department, University of Connecticut, 2152 Hillside Road, U-3046, Storrs, CT 06269, USA. (kharchenko@phys.uconn.edu)

C. M. Lisse, Johns Hopkins University Applied Physics Laboratory, SD/SRE, MP3-E167, 11100 Johns Hopkins Road, Laurel, MD 20723, USA. (carey.lisse@jhuapl.edu)

P. C. Stancil, Department of Physics and Astronomy and the Center for Simulational Physics, University of Georgia, Athens, GA 30602, USA. (stancil@physast.uga.edu)